REVISTA TÉCNICA CIÊNCIAS AMBIENTAIS
IPABHi

Cloud brightness evaluation from ground-based total sky images using the HSV color space parameter

Willian José Ferreira[1,2]; Kátia Celina da Silva Richetto[2], Plínio Carlos Alvalá[1]

[1]Programa de Pós-Graduação em Geofísica Espacial, INPE, São José dos Campos, SP.
[2]Programa de Mestrado em Educação, UNITAU, Taubaté, SP.

willian.jferreira@unitau.br*, katia.csrichetto@unitau.br, plinio.alvala@inpe.br
* Main email for correspondence

ABSTRACT

The RGB color space and two-dimensional red-to-blue band thresholding methods have been widely used for cloud detection throughout history. However, there is a lack of experimental data to assess the nuances of the effectiveness of pixel segmentation techniques in identifying Solar Radiation Enhancement Events (REE). As a result, a study was conducted to correlate surface solar irradiance and cloud pixels during the occurrence of these events, since there is no systematic description of the use of the HSV code parameter to determine cloud brightness in the literature. Therefore, this paper proposes a method to measure image brightness under different sky conditions by integrating the HSV brightness parameter from histograms. Uneven illumination in full-sky images is the most complicated factor in evaluating cloud brightness, as it varies with camera type, local atmosphere, and solar zenith angle. Experimental results show that the proposed algorithm proved effective for the evaluated image set, as satisfactory visual effects were observed under both cloudless and cloudy sky conditions.

Keywords: Cloud detection, Solar radiation enhancement, Pixel segmentation, color space

RESUMO

O espaço de cores RGB e os métodos de limiarização de banda vermelha-azul bidimensional têm sido amplamente utilizados para a detecção de nuvens ao longo da história. No entanto, não existem dados experimentais para avaliar os detalhes da eficácia das técnicas de segmentação de pixels na identificação de eventos de amplificação da radiação solar (REE, na sigla em inglês). Como resultado, foi realizado um estudo para correlacionar a irradiância solar na superfície e os pixels de nuvem durante a ocorrência desses eventos, uma vez que não há descrição sistemática do uso do parâmetro de código HSV para determinar o brilho das nuvens na literatura. Portanto, este artigo propõe um método para medir o brilho de imagens em diferentes condições de céu, integrando o parâmetro de brilho do HSV a partir de histogramas. A iluminação desigual em imagens de céu completo é o fator mais complicador na avaliação do brilho das nuvens, uma vez que varia com o tipo de câmera, a atmosfera local e o ângulo solar de zênite. Resultados experimentais mostram que o algoritmo proposto foi eficaz para o grupo de imagens avaliadas, visto que foram observados efeitos visuais satisfatórios em condições de céu sem nuvens e nublado.

Palavras-chave: Detecção de nuvens, amplificação da radiação solar, segmentação de pixels, espaço de cores

1. INTRODUCTION

Clouds play a critical role in maintaining the energy balance of the atmosphere. The state of their coverage is of immense importance in advancing radiative transfer models and climate simulations, as noted by Yang et al. (2016). These clouds not only affect precipitation, but also significantly influence the arrival of solar radiation at the Earth's surface. This radiation interacts with the atmosphere through scattering and absorption mechanisms, as described by Silva (2022).

In a general sense, a cloud is composed of minute particles of liquid water, ice, or a combination of both, suspended in the atmosphere and typically not in contact with the ground, as highlighted by WMO (2017). Another perspective defines it as a conglomerate of droplets formed from water vapor condensing onto a tiny aerosol particle known as a condensation nucleus, as elucidated by Silva (2022). However, establishing a precise threshold for the number of accumulated droplets that qualifies as a cloud remains elusive. This is especially true given that an aerosol plume, despite its non-spherical particle composition, unlike traditional cloud droplets, can conform perfectly to such a representation, as observed in studies by Chiu et al. (2009) and Koren et al. (2007), cited in Silva (2022).

The most common and widely recognized effect of clouds on solar radiation is attenuation, as shown by Calbó et al. (2017). There is an intriguing cloud phenomenon called a radiation enhancement event (REE) that, under certain circumstances, can lead to an increase in solar irradiance on a surface. During a REE, there is a sudden increase in the radiation flux directed to the ground, resulting from solar radiation scattered by the thinnest parts of the clouds, as described by Parisi and Dows (2004) and Silva et al. (2019).

Silva (2022) elaborates on three different mechanisms that can give rise to REEs: 1) Scattering of solar radiation along the edges of clouds, leading to obscuration; 2) Multiple instances of radiation scattering across the layers of a thin cloud that has the capacity to transmit a significant amount of radiation toward an observer; 3) Solar radiation reflected back into the atmosphere by snow, and the subsequent bouncing back of this reflected radiation, leading to an increase in the total downwelling global radiation.

Despite recent progress in the development of algorithms and techniques for the identification of cloud radiation enhancement events (REEs), their description and quantification based on fundamental physical concepts remains insufficiently precise, especially when considering tropical regions of the world. In addition, there is a need for a deeper understanding of the relationship between the solar irradiance measured at the Earth's surface and the solar brightness scattered by clouds during REEs.

Although human ground-based cloud observations using traditional methods are outdated, they continue to serve as the primary means of collecting cloud cover data in numerous countries (Silva and Souza-Echer, 2016; Yang et al., 2016). Nevertheless, numerous studies have been conducted to improve cloud parameter detection techniques using automated ground-based imaging systems (Silva and Souza-Echer, 2016; Hasenbalg et al., 2020; Logothetis et al., 2022), with a particular focus on advancing REE research. The study of solar brightness scattered by clouds during REE is key to a comprehensive understanding of their influence on the Earth's energy balance, climate patterns, radiative forcing effects, energy production from solar sources, climate modeling accuracy, weather forecasting precision, environmental impacts on ecosystems, and improved interpretation of satellite data for informed decision making and sustainable development.

Essentially, the characterization of cloud brightness by cameras depends on atmospheric illumination, which is determined by factors such as solar zenith angle (SZA) and atmospheric visibility. This assessment is further shaped by the scattering of sunlight by aerosol particles and cloud droplets, as investigated by Wang et al. (2014) and Galileiskii et al. (2015). However,

the challenge of strong forward scattering of sunlight complicates the ability of digital cameras to capture clear sky images, as noted by Yang et al. (2015). These images typically depict clouds in shades of white or gray, largely due to Mie scattering from cloud particles in the visible spectrum, while cloud-free skies have predominantly blue hues due to Rayleigh scattering from atmospheric molecules, as discussed by Yang et al. (2016).

The evaluation of full-sky images typically focuses on the RGB color space and involves the application of two-dimensional red-to-blue band thresholding techniques to distinguish cloud pixels from the sky background, a method used in studies by Heinle et al. (2010), Yang et al. (2015, 2016), and Silva and Souza-Echer (2016). Alongside these approaches, the saturation channel within HSV/HSL/HSI (hue, saturation, value, lightness, and intensity) color spaces has received attention in the literature for detecting cloudiness in images, as described by Souza-Echer et al. (2006), Echer et al. (2006), and West et al. (2014). Despite their promising performance, accurate detection of a cloud's brightness factor remains a complex challenge. In recent years, the effectiveness of HSV-based algorithms for detecting both brightness and small targets in images has been demonstrated by Chen et al. (2007), Hamuda et al. (2017), and Yu et al. (2021), leading to their widespread use in numerous computer vision applications.

Currently, there is a lack of experimental data to evaluate the effectiveness of pixel segmentation techniques in REE studies, as well as a subsequent correlation between surface solar irradiance and cloud pixels. In addition, a systematic review of the use of the HSV color model for cloud brightness assessment is lacking in the literature. Nevertheless, a careful examination of the images suggests a plausible relationship between measured surface irradiance and cloud brightness during such phenomena, which warrants further dedicated investigation.

This paper proposes an algorithm to automatically detect cloud brightness of ground-based total sky images based on the brightness parameter of HSV color space. The concept of imaging and its methodology are described in Sect. 2. In Sect. 3, the brightness variation in sky images is introduced in detail, in addition to an analysis of cloud pixels scattering of solar irradiance in order to validate the proposed method. Finally, a summary and suggestions for future research are provided in Sect. 4.

2. METHODS

2.1 Site description

All full-sky images used in this investigation were acquired within the geographic coordinates of São José dos Campos (SJC), Brazil (23.20º S, 45.86º W, 621 m above sea level), from September 2019 to August 2020. The imaging instrument was placed on a 10 m high structure to reduce potential obstructions from neighboring buildings and trees, while the data acquisition system was located in a room below the instrument. SJC is a medium-sized urban center located between the prominent Brazilian cities of São Paulo and Rio de Janeiro in South America, and is part of the Metropolitan Region conurbation (Portela et al., 2020). Located in the eastern region of the state of São Paulo, SJC holds the distinction of being the largest city in the Paraiba Valley region in terms of fiscal contributions, with a population of 737,310 inhabitants according to the IBGE 2022 census. The city has a humid subtropical (Cfa) climate classification according to the Köppen-Geiger system, characterized by summer rainy periods and winter dry periods, with an average annual air temperature of 20.9°C (Ferreira et al., 2020).

2.2 Device and data

The cloud coverage measurements were performed using a Local Sky Viewer (LSV), a prototype sky imager developed by the Laboratório de Luz Ultravioleta (LLUV/PUC-MG), with a 100° angular aperture that generated local sky images just above the LSV. A CCD digital camera equipped with a 7-8 optical density filter was pointed at the sky to capture 24-bit color Joint Photographic Experts Group (JPEG) images with a resolution of 720 × 576 pixels (415 Kpixel) at a frequency of 20 seconds. This process resulted in the acquisition of 1440 images per day during the 11 a.m. to 7 p.m. Universal Time (UT) interval. Unlike conventional full-sky imagers, the LSV uses a unique technology to capture images of the sky without obstructing the sun. Because the instrument faces both the sky and the sun, it improves the accuracy of cloud identification by accurately detecting clouds that obscure the solar disk.

As pointed out by Cheng et al. (2001), image segmentation is the initial stage of image analysis and pattern recognition. They emphasize that the challenge of image segmentation is fundamentally one of psychophysical perception, and thus doesn't lend itself to a purely analytical solution. For example, humans perceive color as a mixture of tristimuli, often referred to as the three primary colors, a concept explained by Cheng et al. (2001) and Burger and Burge (2009).

Starting from the RGB (Red, Green, and Blue) representation, different color representations (spaces) can be derived through linear or nonlinear transformations (Chaves-González et al., 2010). Among these transformations, the HSI family (HSI, HSL, HSV) uses conic coordinates to represent RGB points (Ibraheem et al., 2012). Within these color spaces, color information is separated from intensity information, with hue (H) and saturation (S) values representing color, while intensity (I, L, and V) describes image brightness, which is determined by the amount of light (Cheng et al., 2001).

Although hue and saturation are consistently defined, the interpretations of intensity, lightness, and value/brightness differ (Cheng et al., 2001). Broadly speaking, the three spaces use slightly different representations for intensity (I), lightness (L), and value (V):

1. Intensity is computed by a simple average of RGB values: $(1/3)\cdot(R+G+B)$.
2. Lightness is an average of the maximum and minimum RGB values: $(1/2)\cdot[\max(R,G,B) + \min(R,G,B)]$.
3. The value is the simplest and represents the maximum RGB value: $\max(R,G,B)$ (Ibraheem et al., 2012).

In both models, the value or lightness of a color does not correspond exactly to the human-perceived lightness. Nevertheless, both value and lightness can approximate brightness in images (Burger and Burge, 2009).

Choosing an optimal color space remains a challenge in image segmentation. However, the choice of the HSV space was influenced by previous research, which found that converting RGB values to grayscale yields suboptimal segmentation results (Tian and Slaughter, 1998; Hamuda et al., 2017). In addition, HSV more closely aligns with human color perception and is more robust to lighting variations than other color models (Sobottka and Pitas, 1996; Burger and Burge, 2009; Chaves-González et al., 2010).

Part of the software architecture was built using the Open Source Computer Vision Library (OpenCV) within the Python programming language. OpenCV, which operates under the Berkeley Software Distribution (BSD) license in its open source version, was chosen for its robust cross-platform capabilities (Bradski and Kaehler, 2008). The selection was based on its advanced application programming interfaces, which enable preprocessing, feature extraction, feature selection, image classifier design, and training. In addition, OpenCV provides a transparent interface that can be dynamically optimized for different processors at runtime (Tian

et al., 2020). With reference to these sources, histograms of the brightness channel within the HSV color space (here denoted as B) were used to assess the discriminability of cloud brightness.

Initially, OpenCV facilitated the use of the cv2.calcHist() function, which is instrumental in calculating color histograms of images. Since the camera image data is represented in terms of primary colors (red, green, and blue), it was necessary to transform the RGB color space into HSV format to directly improve the brightness distribution. This transformation was achieved using the cv2.cvtColor() function, along with the cv2.COLOR_BGR2HSV flag. The latter allowed direct conversion to HSV without the need for an intermediate RGB to grayscale transformation. Next, the HSV histogram (B) of the images was calculated by applying the brightness values to the cv2.calcHist() function. Finally, the region of interest was delineated by integrating B within the histograms to certain limits.

2.3 Segmentation of the LSV image

To test the sensitivity of the algorithm to changes in cloud cover, a set of 30 randomly selected images was first compared using brightness histograms in HSV color space. From different days, 10 images were selected with clear skies and visible sun, 10 images with both sun and apparent clouds, and another 10 images with cloudy skies. All of these images were taken at the same location with identical camera parameters. Representative examples from each set are shown at the top of Figure 1 (a, b, and c).

In Figure 1, the images and data in the leftmost column correspond to April 4, 2020, at 14:50 UT; the middle column corresponds to April 1, 2020, at 16:50 UT; and the third column corresponds to April 1, 2020, at 11:00 UT. The distribution of color intensity in RGB channels is shown in the middle row of the figure (Figures 1d, 1e, and 1f), while the brightness histogram (B) in HSV color space is shown in the bottom row (Figures 1g, 1h, and 1i).

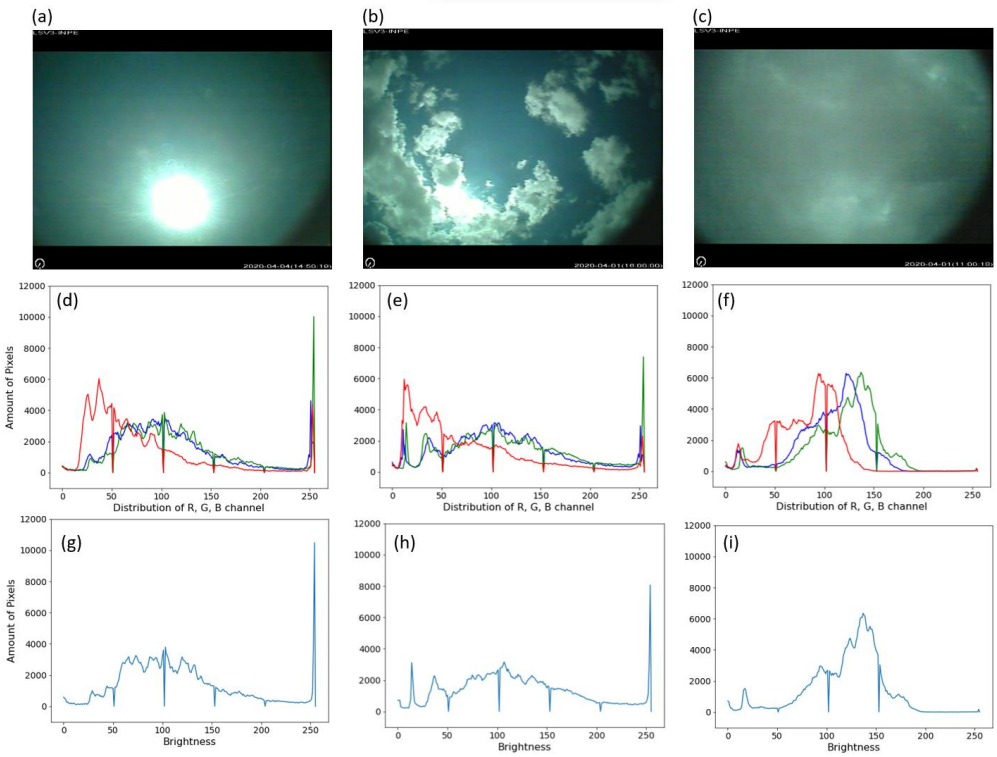

Figure 1. The original three LSV images are shown in the top row (1a, 1b and 1c). The brightness distribution of the RGB channels is on the middle row of the panel (1d, 1e and 1f) and the same in the HSV are on the bottom row (1g, 1h and 1i).

According to Yang et al. (2016), when atmospheric lighting conditions vary between images, their brightness distributions may show significant differences. For example, in Figures 5.14d and 5.14g, the brightness intensity of the solar disk can be seen in the lower-right region of the histograms, with values around 250, as solar pixels tend to be brighter than their surroundings. In Figures 5.14e and 5.14h, an increase in cloud cover in the image results in a reduction of brighter pixels in the same histogram region, a change that is even more pronounced in Figures 5.14f and 5.14i, which show histograms for the cloudy sky image.

In the existing literature, there is no predefined value that defines the threshold for integrating bright pixel values from the Sun (or Sun and clouds) in histograms. Therefore, guided by visual analysis and empirical testing, brightness values (B) above 180, 200, 230, and 245 were considered as threshold criteria for pixel integration.

Figure 2 shows an image of an apparently cloudless sky (a) along with its HSV brightness histogram (b), where the tested segmentation thresholds are marked by red lines. As can be seen from the figure, a lower integration threshold corresponds to an increased number of residual pixels included in the count of bright pixels within the images.

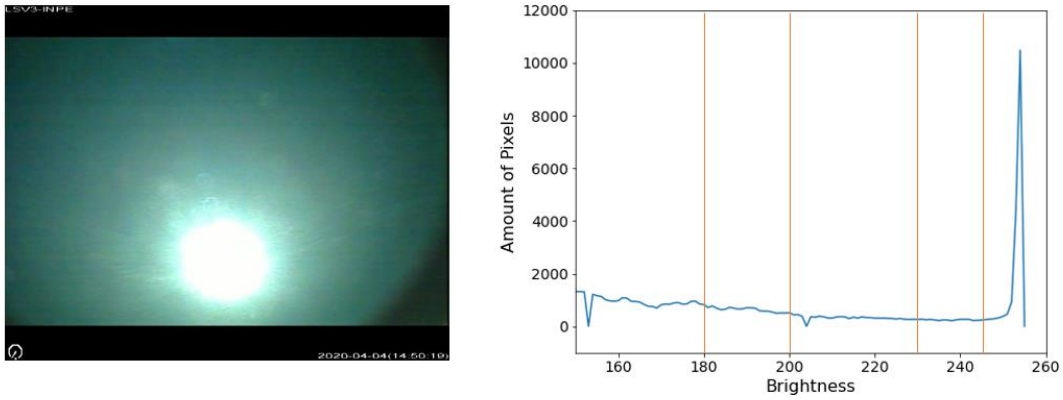

Figure 2: LSV image and its HSV brightness histogram. Red lines represent the threshold of the integration tested in pixel segmentation. Integration criteria: B > 180, B > 200, B > 230 and B > 245.

3. RESULTS

3.1 Solar brightness in a cloudless sky

To assess the algorithm's sensitivity in counting bright pixels, original cloudless sky images were duplicated, and all pixels falling within the brightness threshold range (B) were colored in red. The results are observed in Figures 5.3a (B > 180), 5.3b (B > 200), 5.3c (B > 230), and 5.3d (B > 245). As per Figures 5.3, it can be observed that as the histogram curve to be integrated becomes narrower, the red area in the Figure diminishes (Figures 5.3c and 5.3d).

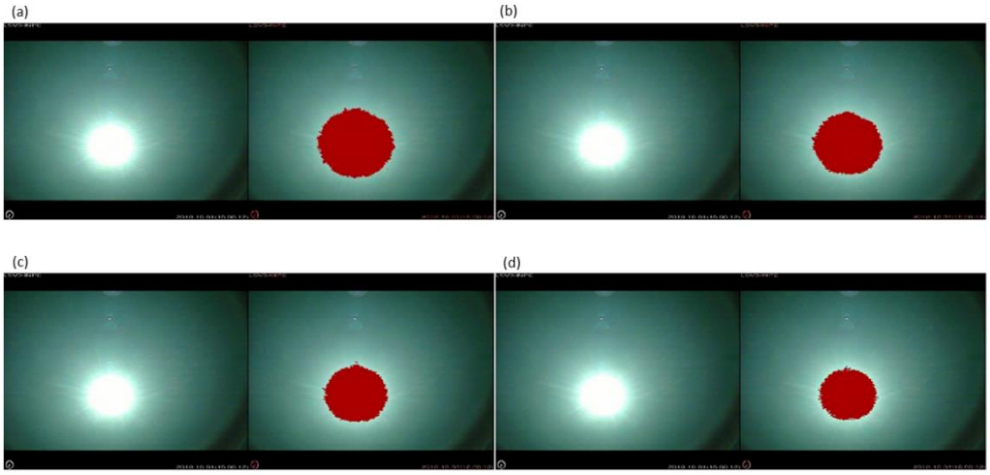

Figure 3: Cloudless sky image and the same image where pixels reflecting the same light intensity were tinted in red (right). A variation in the number of red pixels refers to a change in the integration threshold of the brightness histogram. Integration criteria: Figures 3a (B > 180), 3b (B > 200), 3c (B > 230) and 3d (B > 245).

Looking at the number of red pixels in Figure 3, it is clear that as the parameter B used to integrate the brightness histogram decreases, the number of red pixels in the image increases (Figures 3a and 3b). Conversely, as the integrated curve becomes narrower, a reduction in the red area is observed (Figures 3c and 3d). Daily variations in solar luminosity under cloudless sky conditions were then plotted and compared with results from scientific studies in the literature and radiometer measurements of sky luminosity.

To investigate the possible influence of these thresholds on seasonal brightness, the number of bright pixels in 1440 images taken on cloudless days was counted over four full days, one for each season of the year. The histogram of each image was integrated according to the prescribed procedure for handling brightness intensity. The seasonal variation in the brightness of the cloudless sky images is shown in Figure 4: B > 180 (a), B > 200 (b), B > 230 (c), and B > 245 (d). In Figure 4, the x-axis represents time (UT), the y-axis represents the referenced month, and the z-axis represents the number of bright pixels based on the selected integration criterion.

It's worth noting that the study is located in a tropical region of Brazil, where the sequence of the seasons differs from that of the northern hemisphere. Specifically, spring falls in September, summer in December, fall in March, and winter in June. Regardless of the threshold used, a primary observation emerges: the brightness of a cloudless sky exhibits seasonal variations. This variation is mainly influenced by the interaction of diffuse radiation, as governed by the principles of atmospheric optical thickness (Buglia, 1986).

The characteristic curves obtained in image segmentation process (Figure 4) follows the representation of sky brightness in a cloudless condition captured by instruments (Sakerin et al., 2005; Galileiskii et al., 2015; Priyatikanto et al., 2020).

According to Sakerin et al. (2005), an increase in aerosol optical thickness leads to a higher number of scattering particles, which in turn contributes to the increase in brightness within images. However, an elevated aerosol optical thickness also results in greater extinction of radiation reaching a scattering particle or elementary scattering volume, thus favoring brightness reduction. The authors suggest that the interplay between these two factors could account for the observed variations in sky brightness within images.

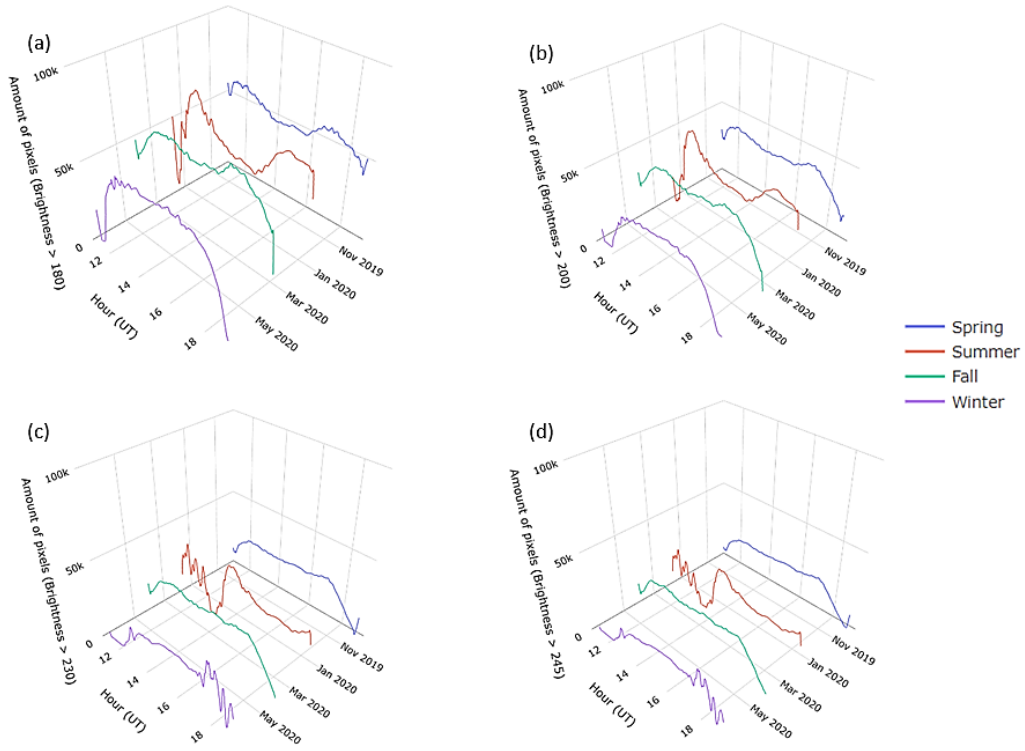

Figure 4: Seasonal variation of brightness pixels in LSV images captured under cloudless sky conditions, with B > 180 (a), B > 200 (b), B > 230 (c) and B > 245 (d).

In Figures 4, in line with Galileiskii et al. (2015), the variation in the brightness of cloudless sky during winter differs from that of summer due to a combination of factors. In many regions, the atmosphere tends to be more stable in winter, accumulating pollutants and suspended particles that lead to the extinction of image brightness. As a result, brightness remains somewhat constant around midday throughout the year. In transitional seasons like spring and autumn, a similar profile of daily brightness variation is maintained, regardless of the chosen brightness parameter (B) for histogram thresholding.

While there could potentially be additional effects on brightness variation due to visually undetected clouds on selected days, a comparison of Figures 4 (a and b) and 5.4 (c and d) reveals, especially for larger Solar Zenith Angles (SZA), that the parameters B > 230 and B > 245 are more sensitive to brightness variations than B > 180 and B > 200.

Consequently, after evaluating how residual pixels in histograms could impact brightness studies in the Enhanced Atmospheric Radiation Sensors (EARS), a statistical analysis was conducted to compare different values used in the bright pixel thresholding process. Based on this assessment, the investigation of brightness variation in images and its relationship with spectral irradiances measured by EARS proceeded using the brightness parameter criterion of B > 245. This criterion corresponds to the region with the least residual bright pixels and encompasses the entirety of pixels located near the central values of pixels with the highest brightness intensity in histograms (B = 250).

3.2 Cloud pixels scattering solar brightness

Having demonstrated the ability of the OpenCV algorithm to quantify pixel counts based on image brightness and to capture daily and seasonal variations in cloudless sky brightness, the same procedure was applied to a collection of partially cloudy sky images. In a

manner analogous to the process used for cloudless sky images, a cloud image was duplicated and all pixels falling within a specified range of brightness (B) were colored red, following the segmentation criterion outlined at the beginning of Section 3.1. The results of this novel processing are shown in Figures 5a (B > 180), 5b (B > 200), 5c (B > 250), and 5d (B > 245).

Visually, the segmentation of the brightness channel (B) to detect cloud scatterers proved to be effective, as evidenced by the red colored pixels in Figures 5. Similar to the cloudless sky scenario (Figure 3), smaller B values correspond to a greater concentration of red pixels within the image (Figures 5a and 5b). Similarly, an increase in B-values corresponds to a decrease in the extent of the reddened area in the integration (Figures 5c and 5d).

In contrast to Figures 3, the most striking aspect of Figures 5 is the expansion of the pixels contributing to brightness. It's obvious that brightness scattering of the same intensity as that of the circumsolar disk occurs at the edges of clouds.

It is also clear that higher B values in the integration result in a count of cloud pixels with an intensity closer to that emitted by the central region of the circumsolar disk (Figures 5c and 5d). It's important to note that choosing lower B values in the integration could lead to miscalculations of image brightness in such investigations.

The validity of the method extends even to cloudy conditions, where it was possible to identify cloud pixels radiating brightness with an intensity similar to the circumsolar disk, even when the Sun wasn't visible in the image. This is important for the study of these phenomena, because contrary to intuition, solar radiation measured on the surface under partly cloudy conditions can show unexpectedly high values compared to cloudless sky days.

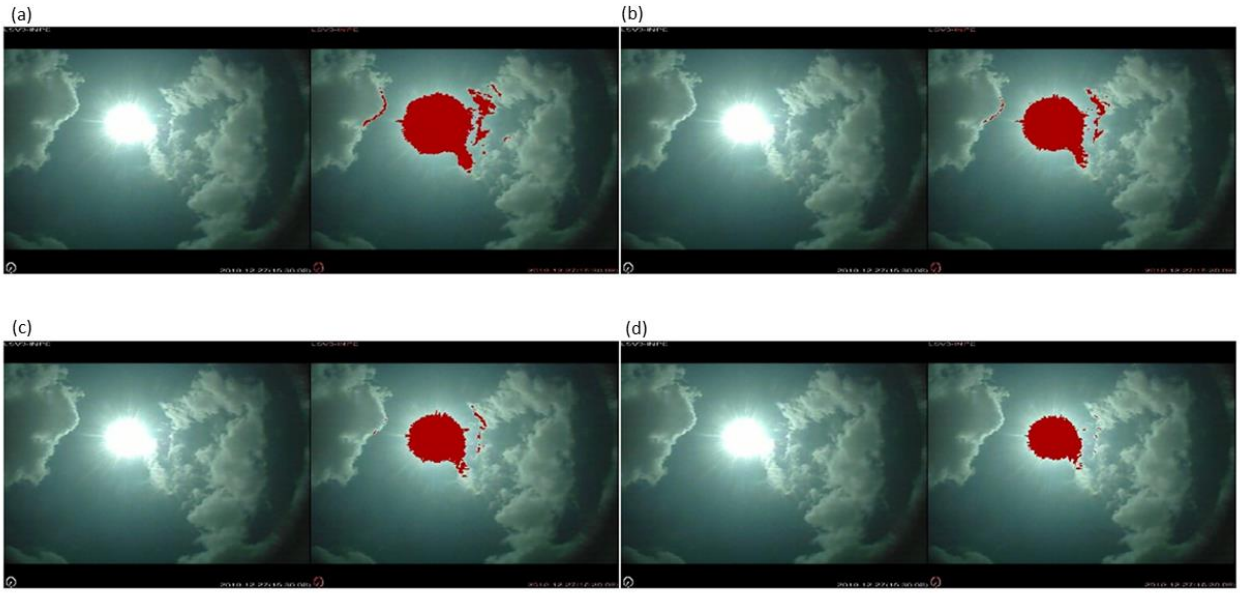

Figure 5: Cloudiness sky image and the same image where pixels scattering the same luminous intensity were tinted red (right). A variation in the number of red pixels refers to a change in the integration threshold of the brightness histogram. Integration criteria: Figures 3a (B > 180), 3b (B > 200), 3c (B > 230) and 3d (B > 245).

In the context of long-term in-situ observations, such as those conducted in the REE studies, a large number of high-quality images can be captured and stored at different solar positions. This approach allows the identification of a corresponding cloud-free sky image for each instance where the solar position is close to or matches that of a cloudy sky image. By excluding the cloudy sky images and focusing on the brightness observed in the cloudless sky images, it becomes possible to compute only the brightness attributed to pixels affected by

cloud scattering. These two images should not only have very similar background brightness distributions, but should also have identical refraction artifacts (Yang et al., 2015).

As a result, OpenCV histograms were found to accurately quantify image brightness in both cloudless and cloudy sky scenarios. Additional assessments suggest that the application of HSV can effectively assess the brightness of different cloud types, providing a critical distinction relevant to REE studies.

4. CONCLUSION

The challenge of accurately assessing cloud brightness stems from the inherent variability in the illumination of sky images. In general, the brightness captured in images depends on factors such as the imaging device used, the solar zenith angle, and the local atmospheric conditions.

The presented approach involves quantifying image brightness under different sky conditions by integrating the value parameter of the HSV color model derived from histograms. The application of this method demonstrated the effectiveness of the algorithm in pixel quantification and its adaptability to different cloudy and clear sky scenarios via a brightness threshold parameter.

As recommendations for future research, merging the results of the 2D red-to-blue methods with the HSV brightness parameter could improve the accuracy of cloud brightness detection. In addition, performing simultaneous sky brightness measurements along with the imaging would allow statistical evaluations of the performance of the computational technique.

Furthermore, it would be valuable to investigate solar brightness and cloudless sky conditions using sensors to establish a correlation with atmospheric transmissivity. Certainly, incorporating measurements of the total optical depth of the atmosphere into this process would refine the methodology, potentially allowing more accurate detection of cloud brightness by directly isolating the circumsolar disk pixels from overcast sky images.

5. REFERENCES

BRADSKI, G., & KAEHLER, A. Learning OpenCV: Computer vision with the OpenCV library. " O'Reilly Media, Inc." Sebastopol, CA, 573p, ISBN: 978-1-78216-392-3, 2008.

BUGLIA, J. J.: Introduction to the theory of atmospheric radiative transfer, Virginia, USA, 180p, NAS 1.61: 1156, 1986.

BURGER, W., BURGE, M.J.: Color Images. In: Principles of Digital Image Processing. Undergraduate Topics in Computer Science. Springer, London. https://doi.org/10.1007/978-1-84800-191-6_8, 2009.

CALBÓ, J., GONZÁLEZ, J. A., BADOSA, J., MCKENZIE, R. and LILEY, B.: How large and how long are UV and total radiation enhancements? AIP Conference Proceedings 1810, 110002, https://doi.org/10.1063/1.4975564, 2017.

CHAVES-GONZÁLEZ, J. M., VEGA-RODRÍGUEZ, M. A., GÓMEZ-PULIDO, J. A., and SÁNCHEZ-PÉREZ, J. M.: Detecting skin in face recognition systems: A colour spaces study. Digital signal processing, 20(3), 806-823, https://doi.org/10.1016/j.dsp.2009.10.008, 2010.

CHEN, W., SHI, Y. Q., and XUAN, G.: Identifying computer graphics using HSV color model and statistical moments of characteristic functions. In 2007 IEEE International Conference on Multimedia and Expo, pp. 1123-1126, https://doi.org/10.1109/ICME.2007.4284852, 2007.

CHENG, H. D., JIANG, X. H., SUN, Y., and WANG, J.: Color image segmentation: advances and prospects. Pattern recognition, 34(12), 2259-2281, https://doi.org/10.1016/S0031-3203(00)00149-7, 2001.

CHIU, J. C., MARSHAK, A., KNYAZIKHIN, Y., PILEWSKI, P. and WISCOMBE, W. J.: Physical interpretation of the spectral radiative signature in the transition zone between cloud-free and cloudy regions, Atmos. Chem. Phys., 9, 1419–1430, https://doi.org/10.5194/acp-9-1419-2009, 2009.

ECHER, M. P., MARTINS, F. R., & PEREIRA, E. B. A importância dos dados de cobertura de nuvens e de sua variabilidade: Metodologias para aquisição de dados. Revista Brasileira de Ensino de Física, 28, 341-352, https://doi.org/10.1590/S1806-11172006000300011, 2006.

FERREIRA, F. L., PEREIRA, E. B. and LABAKI, L. C.: Land surface temperature associated factors in urban areas: local climate zones and spectral characteristics, Amb. Constr., 21, 237-262, https://doi.org/10.1590/s1678-86212021000100504, 2020.

GALILEISKII, V. P., ELIZAROV, A. I., KOKAREV, D. V. and MOROZOV, A. M.: The formation of the sky brightness with horizon position of the sun, Proc. SPIE 9680, 21st International Symposium Atmospheric and Ocean Optics: Atmospheric Physics, 96803L, https://doi.org/10.1117/12.2205504, 2015.

HAMUDA, E., MC GINLEY, B., GLAVIN, M., and JONES, E.: Automatic crop detection under field conditions using the HSV colour space and morphological operations. Computers and electronics in agriculture, 133, 97-107, https://doi.org/10.1016/j.compag.2016.11.021, 2017.

HASENBALG, M., KUHN, P., WILBERT, S., NOURI, B. and KAZANTZIDIS, A.: Benchmarking of six cloud segmentation algorithms for ground-based all-sky imagers, Solar Energy, 201, 596-614, https://doi.org/10.1016/j.solener.2020.02.042, 2020.

HEINLE, A., MACKE, A. and SRIVASTAV, A.: Automatic cloud classification of whole sky images, Atmos. Meas. Tech., 3, 557–567, https://doi.org/10.5194/amt-3-557-2010, 2010.

IBGE. Instituto Brasileiro de Geografia e Estatística, IBGE Cidades. Available online: http://www.cidades.ibge.gov.br (accessed on 2 November 2022).

IBRAHEEM, N. A., HASAN, M. M., KHAN, R. Z., and MISHRA, P. K.: Understanding color models: a review. ARPN Journal of science and technology, 2(3), 265-275, ISSN 2225-7217, 2012.

KOREN, I., REMER, L. A., KAUFMAN, Y. J., RUDICH, Y. and MARTINS, J. V.: On the twilight zone between clouds and aerosols, Geophys. Res. Lett., 34, L08805, doi:10.1029/2007GL029253, 2007.

LOGOTHETIS, S. A., SALAMALIKIS, V., WILBERT, S., REMUND, J., ZARZALEJO, L. F., XIE, Y. and KAZANTZIDIS, A.: Benchmarking of solar irradiance nowcast performance derived from all-sky imagers, Renewable Energy, 199, 246-261, https://doi.org/10.1016/j.renene.2022.08.127, 2022.

MCHUGH, S.: Understanding photography: master your digital camera and capture that perfect photo. No starch press: San Francisco, CA, USA, 240p, ISBN 1593278942, 2018.

PARISI, A.V. and DOWNS, N.: Variation of the enhanced biologically damaging solar UV due to clouds. Photochem. Photobiol. Sci., 3, 643–647, https://doi.org/10.1039/b402035a, 2004.

PORTELA, C. I., MASSI, K. G., RODRIGUES, T. and ALCÂNTARA, E.: Impact of urban and industrial features on land surface temperature: eEvidences from satellite thermal indices, Sustainable Cities and Society, 56, 102100, https://doi.org/10.1016/j.scs.2020.102100, 2020.

PRIYATIKANTO, R., MAYANGSARI, L., PRIHANDOKO, R. A., and ADMIRANTO, A. G.: Classification of continuous sky brightness data using random forest. Advances in Astronomy, p.1-11, https://doi.org/10.1155/2020/5102065, 2020.

SAKERIN, S. M.; ZHURALEVA, T. B. and NASRTDINOV, I. M. Regularities of Angular Distribution of Near-Horizon Sky Brightness in the Cloudless Atmosphere, University of North Texas Libraries, UNT Digital Library, p. 1-8, https://digital.library.unt.edu/ark:/67531/metadc786069/, 2005 (accessed 13 December 2022).

SILVA, A. A. and SOUZA-ECHER, M. P.: Ground-based measurements of local cloud cover, Meteorol. Atmos. Phys., 120, 201–212, https://doi.org/10.1007/s00703-013-0245-9, 2013.

SILVA, A. A. and SOUZA-ECHER, M. P.: Ground-based observations of clouds through both an automatic imager and human observation, Meteorological Applications, 23(1), 150-157, https://doi.org/10.1002/met.1542, 2016.

SILVA, A. A., FERREIRA, W. J., & ALVALA, P. C. Ground-based and Satellite Measurements of Solar Spectral Irradiances at 305 nm and 380 nm at a Tropical Site. Photochemistry and Photobiology, 98, 1245–1251, https://doi.org/10.1111/php.13608, 2022.

SILVA, A. A., YAMAMOTO, A. L. and CORRÊA, M. P.: Daily maximum erythemal dose rates in the tropics, Photochemistry and Photobiology, 95(3), 886-894, 2019.

SILVA, A. A.: Clouds Affecting Total Ozone Column Measurements. Pure Appl. Geophys., 179, 833–844, https://doi.org/10.1007/s00024-021-02931-8, 2022.

SOBOTTKA, K and PITAS, I.: Face localization and facial feature extraction based on shape and color information, Proceedings of 3rd IEEE International Conference on Image Processing, pp. 483-486 vol.3, https://doi.org/10.1109/ICIP.1996.560536, 1996.

SOUZA-ECHER, M. P., PEREIRA, E. B., BINS, L. S., & ANDRADE, M. A. R. A simple method for the assessment of the cloud cover state in high-latitude regions by a ground-based digital camera. Journal of Atmospheric and Oceanic Technology, 23(3), 437-447, https://doi.org/10.1175/JTECH1833.1, 2006.

TIAN, L. F., and SLAUGHTER, D. C.: Environmentally adaptive segmentation algorithm for outdoor image segmentation. Computers and electronics in agriculture, 21(3), 153-168, https://doi.org/10.1016/S0168-1699(98)00037-4, 1998.

TIAN, X., FENG, H., & CHEN, J. An Industrial Production Line Dynamic Target Tracking System Based on HAAR and CAMSHIFT. International Journal of Pattern Recognition and Artificial Intelligence, 34(11), 2059037, https://dx.doi.org/10.1142/S0218001420590375, 2020.

WANG, J., LIU, X., YANG, X., LEI, M., RUAN, S., NIE, K. and LIU, J.: Development and evaluation of a new digital photography visiometer system for automated visibility observation, Atmospheric Environment, 87, 19-25, https://doi.org/10.1016/j.atmosenv.2013.12.045, 2014.

WEI, C.-C., SONG, Y.-C., CHANG, C.-C. and LIN, C.-B.: Design of a solar tracking system using the brightest region in the sky image sensor, Sensors 16, 1995, https://doi.org/10.3390/s16121995, 2016.

WEST, S. R., ROWE, D., SAYEEF, S., & BERRY, A. Short-term irradiance forecasting using skycams: Motivation and development. Solar Energy, 110, 188-207, https://doi.org/10.1016/j.solener.2014.08.038, 2014.

WMO. Manual on the Observation of Clouds and Other Meteors, 2017th ed., WMO-407; International Cloud Atlas, Vol (1). Available online: https://cloudatlas.wmo.int/en/clouds-definitions.html (accessed on 01 November 2022).

YANG, J., MIN, Q., LU, W., MA, Y., YAO, W., LU, T., DU, J. and LIU, G.: A total sky cloud detection method using real clear sky background, Atmos. Meas. Tech., 9, 587–597, https://doi.org/10.5194/amt-9-587-2016, 2016.

YANG, J., MIN, Q., LU, W., YAO, W., MA, Y., DU, J., LU, T. and LIU, G.: An automated cloud detection method based on the green channel of total-sky visible images, Atmos. Meas. Tech., 8, 4671–4679, https://doi.org/10.5194/amt-8-4671-2015, 2015.

YE, L., CAO, Z., XIAO, Y. Deep Cloud: Ground-based cloud image categorization using deep convolutional features. IEEE Transactions on Geoscience and Remote Sensing, 55(10), 5729-5740, 2017.

YU, W., YOU, H., LV, P., HU, Y., and HAN, B.: A moving ship detection and tracking method based on optical remote sensing images from the geostationary satellite. Sensors, 21(22), 7547, https://doi.org/10.3390/s21227547, 2021.